PCCP

ROYAL SOCIETY OF CHEMISTRY

PAPER

Published on 19 November 2026
Licence and permissions

Check for updates

Cite this: DOI: 10.1039/d6cp02947g

Simultaneous gas and condensed phase temperatures to probe synergistic effects of Al/Mg/$KClO_4$-based nanothermites

Qinghui Meng, Keren Shi, Erik Hagen and Michael R. Zachariah *

Received 28th July 2026,
Accepted 19th October 2026

DOI: 10.1039/d6cp02947g

rsc.li/pccp

Al and Mg nanoparticles are widely used fuels in energetic composites but exhibit distinct combustion behaviors. Al provides high energy content compared with Mg, but its performance can be limited by sintering and coalescence. In an Al/Mg blended fuel system, higher volatility of Mg may complement Al. This work investigates synergistic combustion enhancement in physically mixed Al/Mg/$KClO_4$ nanothermites. *In situ* high-speed imaging and emission-based hyperspectral measurements were used to quantify two-dimensional temperature fields near the reaction front, showing that blended fuel containing 70 wt% Al and 30 wt% Mg produced the broadest high temperature region, approximately twice that of Al/$KClO_4$ thermite. The 95th percentile, mean, and median temperatures also peaked at 30 wt% Mg, whereas burn rate peaked at 50 wt% Mg. Further increasing the Mg content above 50 wt% diminished the enhancement. Constant volume pressure cell and calorimetry measurements similarly showed that reactivity and energy release were maximized at 30 wt% Mg. Notably, the pressure rise rate at 30 wt% Mg was 6–7 times greater than those of Al-only and Mg-only formulations. TGA-DSC results showed that Al/Mg powder blend oxidized in two distinct steps, with no evidence of alloying reactions. These results suggest that Mg volatility may contribute to the observed enhancement by acting not only as a fuel but also as a gas-generating component that could mitigate Al coalescence, promote Al vaporization, and enhance overall combustion performance.

1. Introduction

Metal particles are widely used in energetic materials because of their high volumetric energy density, rapid energy release, and tunable reactivity through particle size, morphology, and additive/oxidizer compositions.[1–4] Among metal fuels, aluminum is particularly attractive because of its high heat of combustion, natural abundance, and relatively low cost.[5,6] As a result, micron-sized Al particles have long been used in solid propellants, thermites, and other energetic composite formulations.[7,8]

In recent years, nano-sized aluminum particles (nAl) have attracted increasing attention because their high specific surface area can significantly enhance reaction rates.[3,9] In many reactive systems, nAl exhibits shorter ignition delay, faster burn rates, and more rapid heat release than micron-sized Al.[7,10] However, these advantages are offset by two major limitations: reduced active content due to the oxide shell and a strong tendency for particles to agglomerate during heating.[11,12]

To address these challenges, a variety of strategies have been explored. One major approach is the design of nanostructured composites, which physically separate nAl during heating to suppress agglomeration and improve nanoscale contact with oxidizers.[13,14] For example, nAl has been combined with fluoropolymers,[15–17] gas-generating binders,[18–20] and metal oxides[21,22] to improve dispersion and promote interfacial reactions. Surface modification has also been widely studied as a method to tailor ignition behavior and improve storage stability.[23–26] In addition, alloying Al with other metals or forming metastable intermixed composites have been investigated to alter oxidation behavior, mitigate the constraints imposed by the native alumina shell, and enhance overall reaction rates.[27–29] Although these approaches can effectively reduce the limitations of nAl, they often require additional synthesis steps and careful parameter control. This motivates the exploration of simpler and more scalable strategies.

Beyond Al, magnesium have emerged as another promising energetic metal fuel and have attracted increasing interest because of their high reactivity and low ignition thresholds.[30–32] Although Mg has a lower heat of combustion than Al (Mg: 24.7 kJ g^{-1}; Al: 31.0 kJ g^{-1}),[33] its relatively high volatility at elevated temperatures leads to combustion behavior that differs from Al.[34] This difference suggests that combining nAl and nMg may provide complementary benefits in a simple physically mixed system. Hypothetically, Mg vapor generated during heating may physically

University of California, Riverside, USA. E-mail: mrz@engr.ucr.edu

disrupt particle coalescence, analogous to effects previously reported for gas-generating additives,[18,19] while Al contributes higher overall energy density to the composite.

To examine this possibility, we prepared physically mixed Al/Mg nanoparticle composites spanning a range of Al/Mg ratios and investigated their reaction behavior using a newly developed high-speed pyrometry and hyperspectral imaging system to obtain both the temporal and spatial distribution of both the gas and condensed phase temperatures. These measurements were augmented with ground powder pressure cell measurements, calorimetry, thermogravimetry, differential scanning calorimetry (TGA-DSC) and X-ray diffraction (XRD). The results demonstrate a synergistic effect between nAl and nMg that is not attributed to alloy reactions.

Overall, this work supports the proposed complementary enhancement in Al/Mg nanoparticle composites, establishes a simple route toward more effective use of nAl and nMg, and may inspire future studies on multi-metal fuel systems for energetic materials.

2. Experimental

2.1. Materials

Al and Mg nanoparticles were obtained from US Research Nanomaterials (~100 nm Al, ~800 nm Mg). The active content of Al is 81 wt%, and that of Mg is 76 wt%, as determined from mass gain in TGA under O_2 environment. Details of the TGA measurements are provided in Section 2.6. Potassium perchlorate ($KClO_4$, 99%) was purchased from Alfa Aesar. The polymer binder polyvinylidene fluoride (PVDF, average molecular weight ~534 000) was purchased from Sigma-Aldrich, and hydroxypropyl methylcellulose (HPMC) was purchased from Dow Chemical Company. *N*,*N*-Dimethylformamide (DMF, 99.8%) and hexane were purchased from Fisher Scientific.

2.2. Sample preparation through 3D printing

The complete 3D printing (directly ink writing) process has been reported in previous publications.[35,36] Only a brief description of the procedures and specific parameters used in this study is provided here.

The compositions of the prepared samples are listed in Table 1. To avoid redundancy, in this paper the samples are referred by Al, Mg, or Al : Mg ratios, although the actual formulations are energetic composites containing $KClO_4$ oxidizer and polymer binders. Only the TGA and XRD tests were conducted using solely Al and/or Mg nanoparticles.

To prepare the 3D-printed sample, PVDF and HPMC were fully dissolved in DMF under magnetic stirring, after which $KClO_4$ was added and fully dissolved. Al nanoparticles were then added and mixed using a THINKY AR-100 mixer at 400 rpm for 3 min, followed by sonication for 30 min. Mg nanoparticles were added afterward using the same mixing procedure as for Al. If the sample was printed the following day, the ink was kept under magnetic stirring overnight and sonicated again for 30 min before printing. The nozzle and extrusion parameters for printing were the same as those reported in a previous publication.[36]

2.3. High-speed pyrometry and hyperspectral imaging

We recently developed a new capability to simultaneously obtain the spatial and temporal distribution of both the gas and condensed phase temperature during burning.[36] The system as shown in Fig. 1 is configured as a dual-camera system that integrates hyperspectral emission spectroscopy and three-color pyrometry, enabling simultaneous, high-speed measurements of gas-phase and condensed-phase temperatures. One camera captures the RGB video for three-color pyrometry, while the other captures emission spectra using a mask and diffraction grating system. The camera parameters are listed in Table S1 of the SI. The mask is designed to achieve spatial coverage, allowing for 2D gas-phase temperature profiling. All imaging experiments of composite sticks were conducted in an argon atmosphere.

Gas-phase temperatures are derived using emission spectra based on the Boltzmann equation, utilizing the intensity ratios of potassium emission lines near 580 nm and 693 nm. The spectroscopic parameters used in the calculation were taken from NIST Atomic Spectra Database,[37] and are provided in the SI Table S2. The temperature obtained from this analysis represents the potassium excitation temperature, and is used as an estimate of the local gas translational temperature under local quasi-equilibrium assumption for the selected K I lines. This approximation is supported by the highly collisional environment at 1 atm and around 3500–4000 K. Under this condition, the gas number density is approximately $1.8–2.1 \times 10^{24}$ m^{-3}, and gives heavy particle collision frequencies on the order of $10^8–10^9$ s^{-1}.[38] In the meantime, the selected K I lines upper states have radiative lifetimes about 80–714 ns,[39] corresponding to emission rate on order of $10^6–10^7$ s^{-1}. Therefore, collision relaxation is expected to be faster than radiative decay and supports the Boltzmann distribution.

Table 1 Compositions of the solution for direct ink writing and porosity of printed sample

Sample ID	Polymer binder	DMF [mL]	Al [mg]	Mg [mg]	KClO4 [mg]	Equivalence ratio	Porosity
Al	50 mg PVDF; 75 mg HPMC	4 mL	439.2	—	685.8	1.0	0.362 ± 0.008
Al : Mg = 9 : 1			402.8	44.8	677.5	1.0	0.334 ± 0.057
Al : Mg = 7 : 3			325.7	139.6	659.8	1.0	0.315 ± 0.010
Al : Mg = 5 : 5			242.2	242.2	640.6	1.0	0.381 ± 0.054
Al : Mg = 3 : 7			151.6	353.7	619.8	1.0	0.327 ± 0.011
Mg			—	540.1	584.9	1.0	0.401 ± 0.029

 This journal is © the Owner Societies 2026

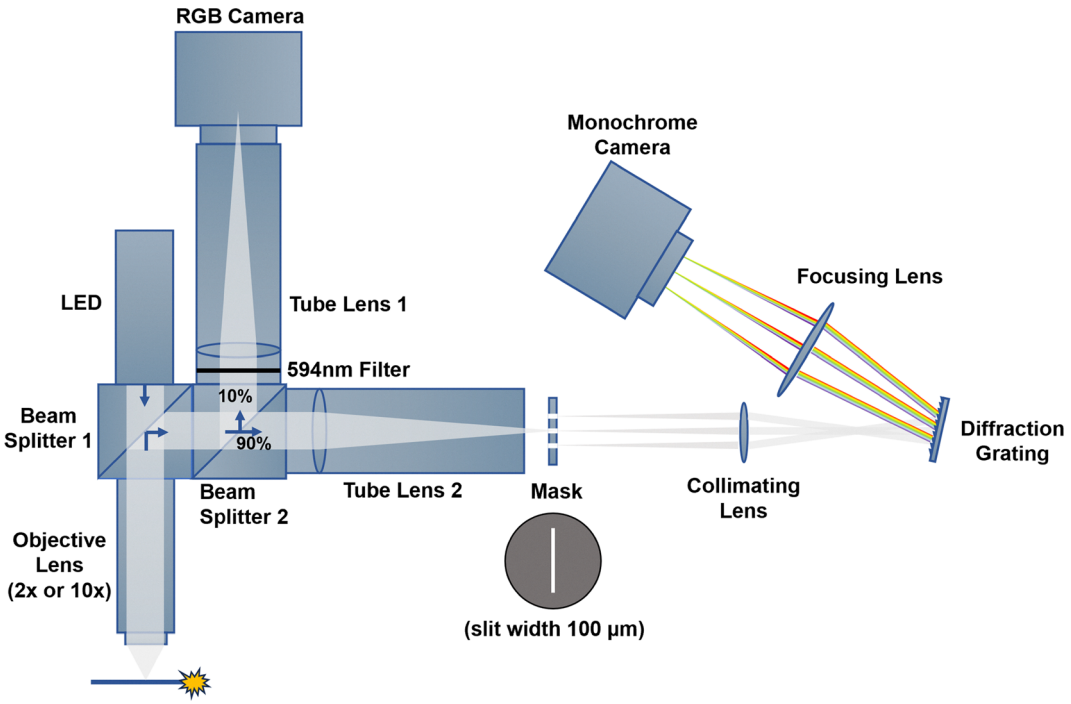


Fig. 1 Schematic of high-speed pyrometry and hyperspectral imaging system.

Three modifications were made compared with previous setup.[36] First, two objective lenses were used in separate measurement: a 2× lens (Mitutoyo 2× Plan Apo) for burn rate and gas temperature field measurement, and a 10× lens (Mitutoyo 10× Plan Apo) for reaction surface imaging and pyrometry. This enabled observations at both global and local scales.

Second, instead of the spatially distributed mask used previously,[36] a single vertical slit mask was used (Thorlabs VA100CP/M, set to 100 μm slit width). This simplified calibration and improved vertical spatial resolution. Assuming steady combustion propagation, the temporal temperature history measured along the slit was converted into a two-dimensional spatial temperature field using the measured burn rate.

Third, the monochromatic camera was operated without an intensifier and instead used on-camera binning mode to improve the signal-to-noise ratio. This simplified the setup and expanded the spectral range from about 350–720 nm to about 350–1000 nm while maintaining sufficient signal for temperature measurements. Although the expanded spectral range was not utilized in this study, it opens the possibility for future measurements requiring broader spectral coverage.

Calibration and spectral data processing followed the procedures described in detail in our previous publication,[36] including the instrumental setup, calibration protocol, spectral resolution, and spectral fitting methodology. For faster processing and noise reduction of hyperspectral images, 10 pixels were averaged vertically, corresponding to about 180 μm in real space, assuming negligible gas-phase temperature variation over this distance. Representative raw spectra, fitted spectra, and fitting residuals at various temperatures are provided in Fig. S1 of the Supplementary Materials. Same as in previous publication,[36] uncertainty was determined from the fitting confidence interval, and data points with uncertainty greater than 350 K were excluded. It should be noted that, the reported temperature trends are more important for reflecting the combustion behavior of the samples, whereas the absolute temperature values may be affected by systematic errors arising from the calibration source and from uncertainties in the spectroscopic parameters adopted from the NIST database. As discussed in our previous work,[36] the use of different databases can result in significant differences in the inferred temperatures.

2.4. Pressure cell tests

Details of the pressure cell measurements are described previously.[40] The 3D-printed thermite sticks were manually ground to powder in hexane and then vacuum-dried before being loaded into the pressure cell.

2.5. Calorimetry tests

The energy release of printed composites with varying Al : Mg ratios were measured using a semimicro calorimeter (Parr Instrument Company, model 6725). The calorimeter was calibrated using the heat of combustion of ~200 mg benzoic acid tablets to determine the energy equivalent. For the composites test, ~40 mg of printed composites were loaded in a 22 mL combustion vessel. The vessel was purged with argon at ~14 atm for five times to remove residual air and then filled ~1 atm argon prior to ignition. Ignition was achieved using a nichrome wire. After each measurement, the contribution of the ignition wire to the total heat release was corrected by measuring the remaining wire length and subtracting from corresponding energy.

2.6. TGA-DSC

TGA measurements were used to determine the active contents of Al and Mg nanoparticles and to investigate whether any evidence of alloy reactions exist between them. A Netsch STA 449 F3 Jupiter TGA-DSC system was used. As-received Al and Mg nanoparticles were tested, and Al/Mg mixtures were prepared by sonication in hexane followed by vacuum drying. For all experiments, 1–1.5 mg of powder was loaded and heated in O_2 at a heating rate of 10 K min^{-1}. For alloy-reaction assessment, the maximum temperature was 1273 K. For active-content determination, the samples were heated to 1473 K and held at that temperature for 1 h.

2.7. X-ray diffraction measurement

The combustion products from different composites were collected and the composition were characterized by X-ray diffraction (PANalytical Empyrean Series 2) with Cu Kα radiation source from 10 to 80° with 0.01° step size.

3. Results and discussions

3.1. 2D Temperature results from hyperspectral and pyrometry imaging

Fig. 2 presents results from the high-speed imaging measurements obtained with the lower-magnification configuration (2× objective) of a composite burning from right-to-left. The left panels show representative snapshots from the color camera. In all cases, the reaction surface appears approximately conical, with the cone angle tending to decrease as the Mg fraction in the fuel increases. A luminous plume near the surface indicates the gas-phase reaction zone, with emissions arise from a combination of thermal radiation and atomic/molecular emissions. The plume contains condensed reaction products (Al_2O_3, MgO, KCl, *etc.*), as well as molten and partially reacted Al particles. Based on the images, increasing the Mg content up to about 30 wt% appears to broaden the reaction zone, whereas at 50 wt% Mg and above, the plume size decreases substantially.

The burn rates derived from the color videos are summarized in Fig. 3 and were also used to convert the temporally resolved gas-phase temperature measurements from hyperspectral imaging into spatial profiles (Fig. 2, middle panels). As mentioned in methodology, temperatures were filtered using an uncertainty threshold of 350 K. The measured temperatures are also shown as normalized histograms (Fig. 2, right panels) to highlight their statistical distributions, with the median and mean indicated by vertical lines.

The 2D temperature fields are broadly consistent with the snapshots, supporting the assumption of quasi-steady reaction and use of the measured burn rates to convert time to space. As a simple comparative metric, the high temperature zone is defined as the largest continuous region where the temperature is higher than 3500 K. The reported uncertainties of high temperature areas below are the standard deviations of three repeated measurements. For the mixed-fuel compositions, partial replacement of Al by Mg below 50 wt% is showing an apparent enhancement in combustion, as indicated by an extended high-temperature region and increased burn rate. The high temperature zone grows from 11.2 ± 1.2 mm^2 for pure Al to 23.6 ± 5.6 mm^2 for Al : Mg = 7 : 3, roughly a twofold increase. At higher Mg fractions, however, the temperature fields show smaller reaction zones and drops of peak temperatures. At 50 wt% Mg, the area of temperature zone above 3500 K decreases dramatically to 8.1 ± 4.6 mm^2. As the Mg exceeds 50 wt%, the high temperature area over 3500 K diminishes continuously and drops to 4.8 ± 2.7 mm^2 in the pure Mg case. This trend is also reflected in the temperature histograms, where the medium and mean shift toward higher temperatures at mass ratio Al : Mg = 7 : 3 and then move back toward lower temperatures with further Mg addition. Fig. 3 summarizes the 95th percentile temperatures obtained from the temperature fields. 95th percentile temperatures increase from approximately 3788 ± 139 K to 4174 ± 153 K when Mg content in fuel increases from 0 wt% to 30 wt%, then decrease with more Mg until about 3527 ± 37 K for pure Mg.

As shown in Fig. 3, the measured burn rates of the pure Al and pure Mg thermites are nearly identical, with Al at 6.3 ± 0.3 cm s^{-1} and Mg at 6.4 ± 0.7 cm s^{-1}. Since both single metal thermite have the same burn rate, a non-interacting mixture at any blend ratio would be expected to burn at approximately the same rate. However, the blended formulations significantly exceed this baseline. At 70 wt% Al and 30 wt% Mg, the burn rate is 10.05 ± 0.2 cm s^{-1}, which is 59% higher than pure metal case. It continuously increases to 12.3 ± 0.7 cm s^{-1} at Al : Mg = 5 : 5, after which it drops rapidly as the Mg fraction increases further. This non-monotonic trend confirms that the enhancement arises from a coupled interaction between Al and Mg during combustion rather than from the independent contribution of each metal fuel.

A 10× objective lens was used to further magnify the reaction surface, enabling visualization of finer surface features and pyrometry measurements. The corresponding results are shown in Fig. 4, with averaged condensed phase temperatures plotted in Fig. 3 for comparison with gas phase temperatures. In all cases, the condensed phase temperatures from pyrometry are 2500 ± 200 K, which are much lower than gas-phase temperatures. The measurements indicate that a substantial portion of the heat release occurs above the surface and therefore the reactions are gas-phase dominant, as proposed in early research[41] and discussed previously.[36]

For the Al-rich sample, micron-scale droplets are visible on the reaction surface. After the droplets leaving the surface, they often keep reacting and surrounded by a nanoparticle cloud when they are still in reaction zone. In contrast, the Mg-rich sample exhibits a darker surface appearance with fewer condensed droplets, which may be associated with the greater volatility of Mg.

3.2. Constant volume measurements for pressurization and energy

Fig. 5 shows constant-volume measurements for Al/Mg/$KClO_4$ reactions, including pressure cell and calorimetry results. The

 This journal is © the Owner Societies 2026

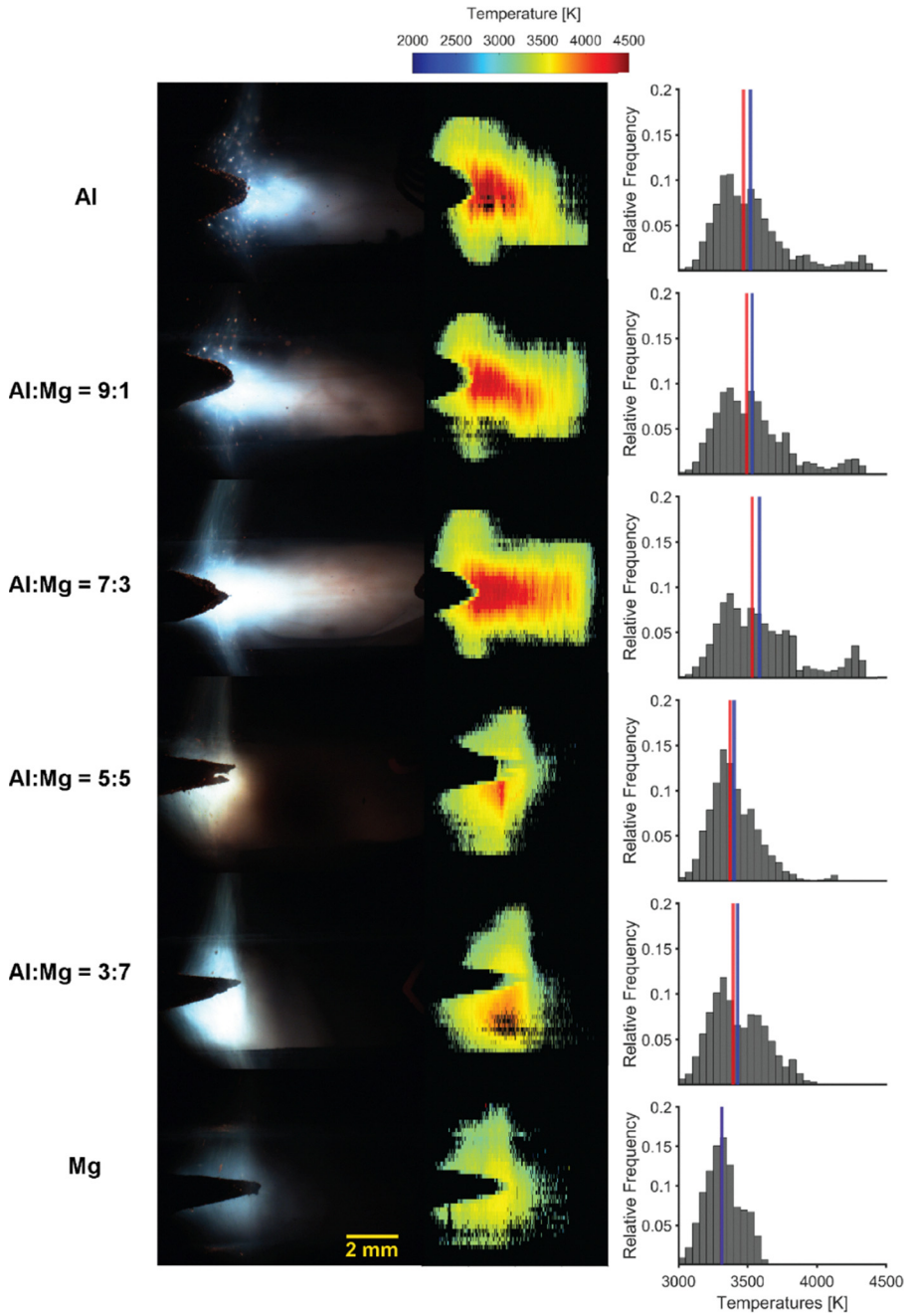


Fig. 2 Snapshots of the lower-magnification reaction fields (left) filtered 2D gas-phase temperature profiles (middle), and temperature histograms (right). The snapshots and gas temperature profiles are shown at the same scale, as indicated by the yellow scale bar. The vertical lines in the histograms represent the median (red) and mean (blue) of the measured temperatures.

pressure cell tests provide the peak pressures (P_{max}) and pressure rise rates (dP/dt). The reader is reminded that for these tests, the composite was ground to a powder. Compared with the pure Al case, pure Mg exhibits a higher peak pressure at 511 kPa and pressure rise rate at 197 kPa ms^{-1}, while those of Al are 271 kPa and 161 kPa ms^{-1}. This result is consistent with the higher volatilization tendency of Mg. For the mixed Al/Mg cases, even a small Mg addition substantially changes the pressure response. With only 10 wt% Mg in the fuel, the peak pressure increases to 489 kPa, which is approximately 80% higher than that of the pure Al case. This result suggests that small Mg addition is an effective strategy to significantly enhance the pressure output of Al-based formulations. For Al : Mg mass ratios ranging from 7 : 3 to 3 : 7, the peak pressure do not increase dramatically compared with the pure Mg case. However, all mixed compositions exhibit higher pressure rise rates than pure Mg. The maximum pressure rise rate is observed at Al : Mg mass ratio of 7 : 3, reaching 1241 kPa ms^{-1}, which is approximately 6–7 times higher than those of the pure Al and Mg cases.

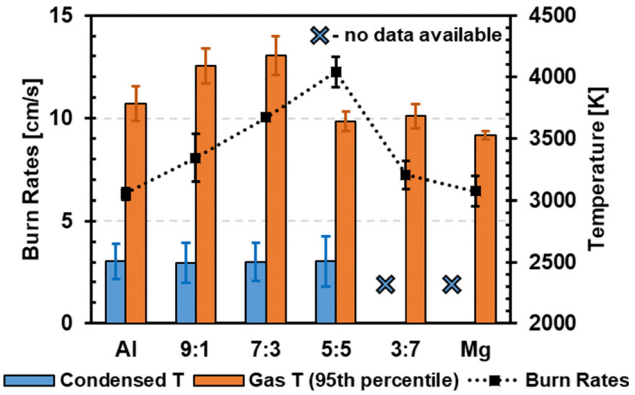


Fig. 3 Burn rates (line plot), averaged condensed phase temperatures (blue bars) and 95th percentile gas phase temperatures (orange bars) of Al/Mg/KClO4 thermites as a function of Al : Mg mass ratio. Error bars indicate standard deviations from three tests per sample.

The calorimetric measurement shows similar trends. When Al and Mg were used as fuel alone, the energy release from the composites were 6670 and 5970 J g^{-1} respectively. The energy release increased when mixing Al and Mg and peaks at 7 : 3 mass ratio.

These results confirm a synergistic interaction between Al and Mg in the constant-volume environment. The energy release should decrease monotonically with increasing Mg content given the lower heat of combustion of Mg, yet the measured values increase and peak at the Al : Mg = 7 : 3 ratio, indicating that blending promotes more complete combustion. Similarly, the pressure rise rates of pure Al and pure Mg are comparable (161 and 197 kPa ms^{-1}), so a non-interacting mixture would be expected to yield similar values at any blend ratio. Instead, all blended formulation exceeds that baseline well outside experimental uncertainty. These evidences clearly demonstrate that the interaction between Al and Mg enhances combustion beyond what each metal contributes independently.

3.3. TGA-DSC verifying no alloy reactions before and during oxidation

Fig. 6 shows the TGA-DSC results for the oxidation of nMg/nAl mixtures in O_2. The vertical dotted lines correspond to the pure metal cases with nMg begins to oxidize at approximately 400–450 °C, and nAl begins to oxidize at around 550 °C. For the mixed systems the DSC is probably the most illuminating. Two distinct oxidation heat flow are observed, with an Mg oxidation exothermic peak near 530 °C and Al oxidation exothermic peak

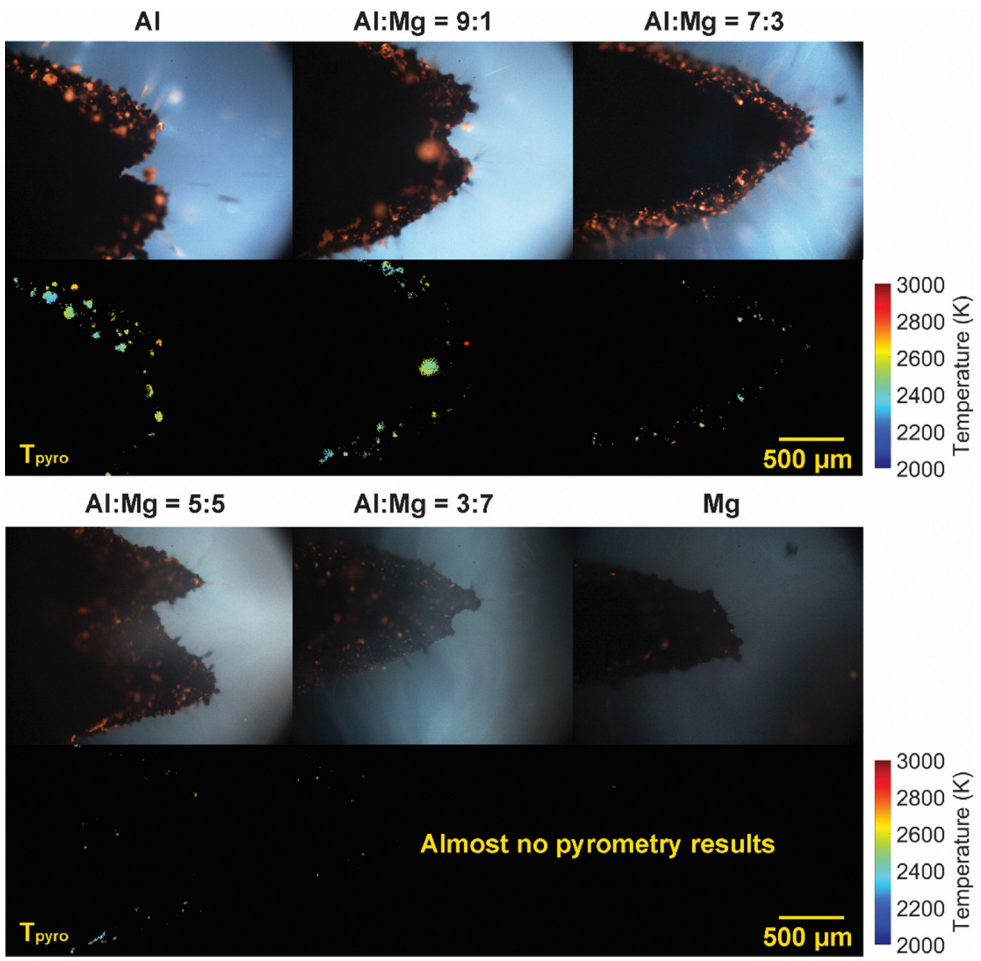


Fig. 4 High-magnification snapshots (top) and pyrometry results (bottom) of the reaction surface.

This journal is © the Owner Societies 2026

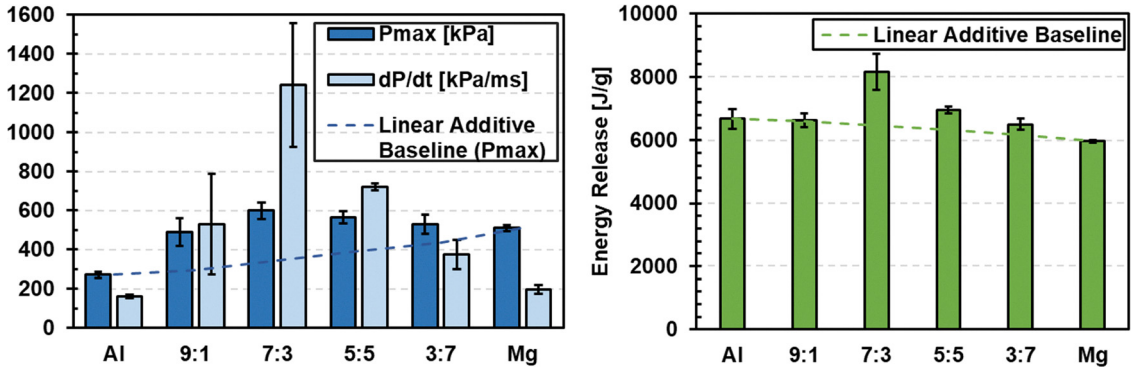


Fig. 5 Pressure cell (left) and calorimetry (right) measurement results. The linear additive baseline represents the reference response from the independent contributions of Al and Mg, assuming no synergistic interaction between them.

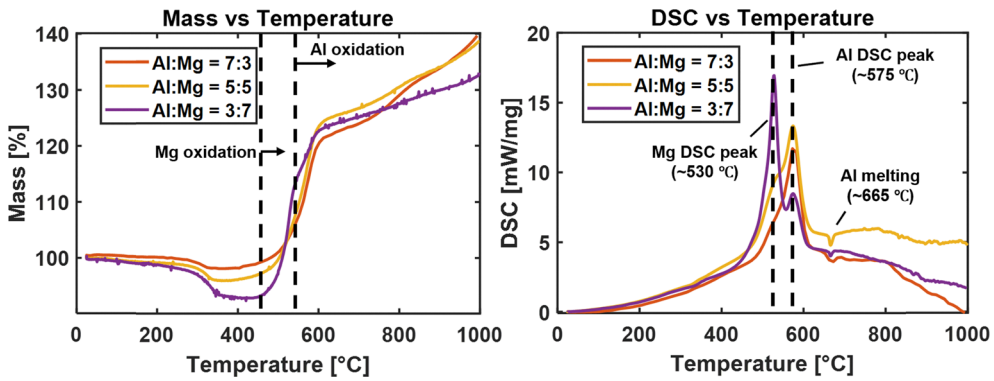


Fig. 6 TGA-DSC curve of mixed Al/Mg nanoparticles in O_2 environment. The dashed lines mark where oxidation starts for pure nMg and nAl case.

near 575 °C. The relative intensities of these peaks vary with the Al : Mg mass ratio. A small endothermic peak at approximately 665 °C indicates the melting of Al, while no obvious endothermic peak corresponding to Mg melting is observed. Overall, the TGA-DSC results suggest that Mg and Al oxidize sequentially, with no clear evidence of alloying reactions.

3.4. Combustion product analysis

Fig. 7 shows the XRD of constant-pressure thermite combustion products obtained from samples with different Al : Mg fuel ratios. In the pure Al case, residual crystalline Al is observed in the products, indicating incomplete consumption of Al, which is consistent with particle agglomeration during combustion. The absence of Al_2O_3 peaks is attributed to its amorphous phase. For the sample with only Mg as fuel, MgO is clearly detected while no residual Mg is observed, suggesting more complete oxidation. This observation is consistent with the higher reactivity of Mg from the pressure cell measurements. In the mixed Al/Mg systems, no Al/Mg alloy phase is detected in the combustion products, consistent with the TGA results indicating no detectable alloy formation prior to oxidation. In contrast, the presence of $MgAl_2O_4$ is identified, indicating interactions between Al- and Mg-containing species during high-temperature gas-phase oxidation and subsequent product condensation. These findings suggest that the enhanced combustion behavior is not driven by pre-oxidation alloy reaction, but rather by the physical and chemical interactions occurring during combustion.

4. Discussion

The results of this study clearly demonstrate a synergistic enhancement of Al and Mg combustion in Al/Mg/$KClO_4$ energetic composite systems, as supported by high-speed imaging, hyperspectral gas-phase temperature measurements, and constant-volume tests. The burn rate, pressurization rate and energy release of blended formulations all significantly exceed the baselines established by the pure Al and pure Mg cases, confirming that this enhancement arises from a coupled interaction instead of the independent contribution of each metal. The combustion enhancement observed in Al/Mg mixtures is suggested to be a combined result of reaction kinetics, heat transfer, mass transport and phase changes. Table 2 compares the thermal properties of Al and Mg. Although Al has a higher heat of combustion and adiabatic flame temperature than Mg, incomplete Al consumption limits the energy release. By contrast, the boiling point of Mg (1363 K) is much lower than the surface temperatures (2500 K, with Al presents) measured by pyrometry. Therefore, Mg is expected to vaporize rapidly at the surface. The early vaporization and oxidation of Mg can provide

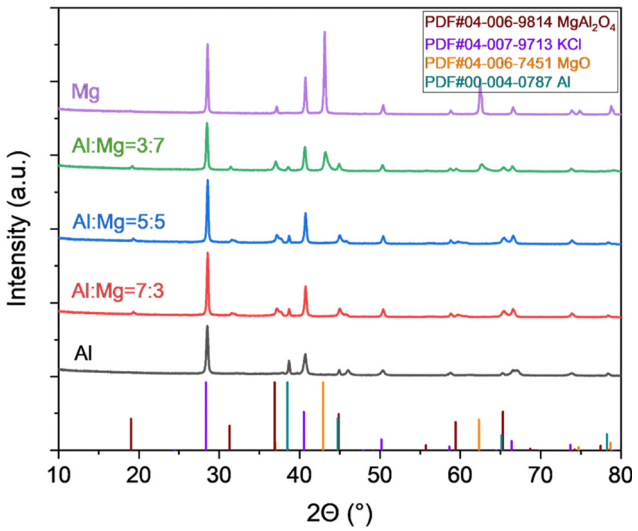


Fig. 7 XRD results of combustion products at different fuel ratios.

localized heat release and gas generation, which is consistent with enhanced Al heating, melting and vaporization. In this way, Mg not only acts as an energetic fuel, but also appears to increase the fraction of Al participating in gas phase oxidation.

The measured burn rate trend suggests that the flame propagation is governed by upstream heat feedback from the hot reaction zone to the unreacted material, as well as the properties of the material. Heat released by gas phase oxidation transfers to preheating zone, and sustains $KClO_4$ decomposition, metal melting and vaporization. As a greater fraction of fuel participates in near-surface combustion, the heat feedback increases flame propagation until a thermal balance is reached. However, the present results further indicate that the peak temperature near the reaction surface and the material properties could be more influential than the area of the hot zone. This explains why the largest hot zone area was observed at Al : Mg = 7 : 3, but the maximum burn rate was observed at Al : Mg = 5 : 5. At the ratio of 5 : 5, the gas temperature decreases only modestly while the higher Mg content likely continued to accelerate vapor generation and mass transport. When Mg exceeded 50 wt%, the measured peak gas temperature further decreases, reducing heat feedback and causing the burn rate to decrease.

Fig. 8 illustrates the proposed mechanism. In the pure Al case, micron-sized molten droplets form on the reaction surface and coalesce before leaving the surface. Because the gas-phase reaction zone is spatially limited, the Al droplets' residence time within the high-temperature region is short. Once the droplets leave the reaction zone, their combustion is expected to terminate due to insufficient O_2 and lower temperature. As a result, larger ejected droplets likely retain a substantial fraction of unreacted Al, reducing the overall combustion efficiency.

High-speed imaging (Fig. 2 and 4) shows that the size of Al droplets on the reaction surface decreases as Mg replaces Al in the fuel. Although this trend is partly attributable to the lower Al content in the formulation, the composition changes alone cannot explain the observed expansion of the reaction zone and the increased burn rate when less than 50 wt% Mg replaces Al. Multiple independent observations support the interpretation that volatile Mg acts as both a gas-generating component and as an early heat releaser that enhances Al evaporation while mitigating nanoparticle sintering and droplet coalescence. As more Al vaporizes and participates in near-surface gas-phase reactions, more heat is released in the reaction zone, leading to an expanded high-temperature region and stronger heat feedback to the preheating zone.

However, as the Mg fraction increases further, the enhancement gradually diminishes because the Al content becomes lower. Even if a large fraction of the available Al participates in the reaction, the total heat released associated with Al oxidation is limited by its reduced mass fraction. As a result, both the burn rate and flame temperature decrease and shift toward those of the pure Mg case. This trend indicates that the optimized synergistic enhancement depends on a balance between the volatility of Mg and the energy contribution of Al.

The synergistic effect is also observed in constant-volume reactions, as reflected by the pressure cell measurements and calorimetry. The higher peak pressure and pressure rise rate of Mg demonstrate its greater volatilization relative to Al. Moreover, the mixed Al/Mg formulations exhibit greatly enhanced pressure rise rates and energy release, supporting the proposed mechanism that Mg promotes more rapid pressurization and more effective participation of Al in the reaction. The complementarity of these results is to be noted, since in the calorimeter case we have a propagating flame that relies on heat feedback while in the constant volume pressure cell we have powder burning, where heat flux effects are very different. This

Table 2 Thermochemical properties of pure Al and Mg[42]

Property	Unit	Al	Mg
Heat of combustion[33]	kJ g^{-1}	31.0	24.7
Adiabatic flame temperature (with $KClO_4$, const. P)[a]	K	3826	3355
Adiabatic Flame Temperature (with O_2, const. P)[b]	K	3969	3391
Melting point	K	933	922
Boiling point	K	2793	1363
$c_{p,s}$ (at 298 K)	J g^{-1} K^{-1}	0.90	1.02
$c_{p,l}$	J g^{-1} K^{-1}	1.18	1.41
Heat of fusion	J g^{-1}	397	349
Heat of vaporization	kJ g^{-1}	10.9	5.3

[a] Calculated from Cheetah,[43] phi = 1, initial condition 298 K, 1 atm. [b] Calculated from NASA CEA,[44] phi = 1, initial condition 298 K, 1 atm.

This journal is © the Owner Societies 2026

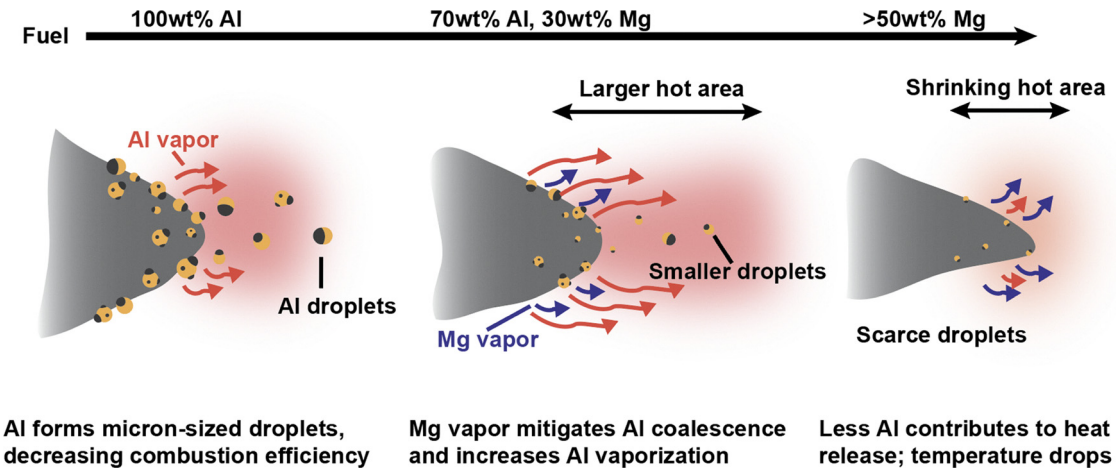


Fig. 8 Diagram illustrating the synergistic effect between Al and Mg.

implies that the burning enhancement with added Mg is not directly related to heat feedback from the pre-heat zone of a deflagrating solid, further supporting a volatility-driven interaction mechanism.

Another possible explanation for the combustion enhancement is alloy-related reaction pathways. To examine the potential role of alloy reactions, TGA-DSC and XRD measurements were performed. However, the results do not support this interpretation. TGA-DSC measurements show no alloying reactions or the formation of Al/Mg/O alloy phases under oxidation conditions, while $MgAl_2O_4$ presence in combustion products from mixed fuel conditions, suggesting it forms during combustion rather than through pre-reaction alloying. Therefore, the observed enhancement is more likely attributable to physical interactions between Mg volatilization and Al evaporation, rather than to alloy formation. We note that detailed multiphase combustion modeling would be needed to fully decouple the contributions of individual variables, such as particle size and microstructures. Such modeling is beyond the scope of this work, but represents a valuable direction for future study.

5. Conclusions

In this work, we investigated the synergistic effects of physically blended Al and Mg nanoparticle fuels in $KClO_4$-based energetic composites. Based on the experimental observations, we proposed a combustion-enhancement mechanism: Mg volatilization mitigates Al sintering and coalescence while promoting Al vaporization, increasing the overall combustion performance. Two-dimensional temperature profiles obtained from high-speed pyrometry and hyperspectral imaging clearly showed an expanded gas-phase reaction zone for blended Al/Mg fuels. The most pronounced enhancement was observed at an Al : Mg mass ratio of 7 : 3, which produced a high-temperature region approximately twice that of the Al-only formulation. The 95th percentile, mean, and median temperatures also reached their maxima at this Al : Mg = 7 : 3 ratio. Magnified reaction surface snapshots further showed reduced droplet coalescence size in the blended-fuel formulations, supporting the proposed interaction between Mg volatilization and Al combustion.

Constant-volume pressure cell and calorimetry measurements further showed that Mg exhibits stronger volatilization-driven pressurization behavior than Al, and demonstrated that the synergistic effect is not limited to constant pressure combustion but also occurs in confined constant-volume environment. In particular, the pressure rising rate of the Al : Mg = 7 : 3 formulation was 6–7 times greater than those of the Al-only and Mg-only samples.

Finally, TGA-DSC and XRD analyses were used to evaluate whether Al–Mg alloy reactions could explain the enhancement. Because these measurements show no clear evidence of alloy formation during heat-up process, the observed combustion enhancement is more likely attributed to the physical interaction between Mg vaporization and Al reaction.

Overall, this work demonstrates that the properties and combustion behaviors of different metals can complement one another when combined in an energetic composite system. In the case of this study, the high volatility of Mg and the high energy content of Al work together to produce a strong synergistic enhancement in energy release. This finding suggests a simple and effective strategy for maximizing the performance of Al and Mg nanoparticles as energetic fuels, while also improving fundamental understanding of the combustion behavior of each individual metal.

More broadly, similar synergistic effects may exist in other multi-metal energetic systems. Exploring such combinations could not only identify formulations with improved combustion characteristics, but also deepen mechanistic understanding of metal nanoparticle fuels. This knowledge can support the design and optimization of future energetic materials and other metal nanoparticle based reactive systems.

Conflicts of interest

There are no conflicts to declare.

Data availability

Data will be made available upon reasonable request.

Supplementary information (SI) is available. See DOI: https://doi.org/10.1039/d6cp02947g.

Acknowledgements

This research was supported by the Department of Defense, Defense Threat Reduction Agency (DTRA) under the MSEE URA (Grant HDTRA1-20-2-0001).

References

1 P. M. Gandhi, M. Schoenitz and E. L. Dreizin, Evaluation and design of metal-based gas-generating energetic materials, *Combust. Flame*, 2023, **249**, 112615.
2 E. V. Bukovsky, R. V. Reeves, A. Krish, A. E. Gash and N. G. Glumac, Experimental study of structure/behavior relationship for a metallized explosive, in *AIP Conf. Proc.*, AIP Publishing LLC, 2018, p. 150006.
3 R. A. Yetter, G. A. Risha and S. F. Son, Metal particle combustion and nanotechnology, *Proc. Combust. Inst.*, 2009, **32**, 1819–1838.
4 N. H. Yen and L. Y. Wang, Reactive metals in explosives, *Propellants, Explos., Pyrotech.*, 2012, **37**, 143–155.
5 W. Pang, L. T. DeLuca, A. A. Gromov and A. S. Cumming, *Innovative Energetic Materials: Properties, Combustion Performance and Application*, Springer, 2020.
6 E. I. Shkolnikov, A. Z. Zhuk and M. S. Vlaskin, Aluminum as energy carrier: Feasibility analysis and current technologies overview, *Renewable Sustainable Energy Rev.*, 2011, **15**, 4611–4623.
7 L. Meda, G. Marra, L. Galfetti, F. Severini and L. De Luca, Nano-aluminum as energetic material for rocket propellants, *Mater. Sci. Eng., C*, 2007, **27**, 1393–1396.
8 D. G. Piercey and T. M. Klapötke, *Nanoscale Aluminum - Metal Oxide (Thermite) Reactions for Application in Energetic Materials*, (n.d.).
9 E. L. Dreizin, Metal-based reactive nanomaterials, *Prog. Energy Combust. Sci.*, 2009, **35**, 141–167.
10 L. Galfetti, L. T. DeLuca, F. Severini, G. Colombo, L. Meda and G. Marra, Pre and post-burning analysis of nano-aluminized solid rocket propellants, *Aerosp. Sci. Technol.*, 2007, **11**, 26–32.
11 K. Jayaraman, S. R. Chakravarthy and R. Sarathi, Accumulation of nano-aluminium during combustion of composite solid propellant mixtures, *Combust., Explos. Shock Waves*, 2010, **46**, 21–29.
12 X. Liao, J. Pei, P. Xie, Y. Hu and J. Liu, Aluminum particle agglomeration characteristics and suppression method during the combustion of aluminum-based solid propellants: A review, *Propellants, Explos., Pyrotech.*, 2024, **49**, e202300131.
13 N. V. Muravyev, K. A. Monogarov, U. Schaller, I. V. Fomenkov and A. N. Pivkina, Progress in additive manufacturing of energetic materials: Creating the reactive microstructures with high potential of applications, *Propellants, Explos., Pyrotech.*, 2019, **44**, 941–969.
14 H. Wang, R. J. Jacob, J. B. DeLisio and M. R. Zachariah, Assembly and encapsulation of aluminum NP's within AP/NC matrix and their reactive properties, *Combust. Flame*, 2017, **180**, 175–183, DOI: 10.1016/j.combustflame.2017.02.036.
15 Y. Jiang, Y. Wang, J. Baek, H. Wang, J. L. Gottfried, C.-C. Wu, X. Shi, M. R. Zachariah and X. Zheng, Ignition and combustion of Perfluoroalkyl-functionalized aluminum nanoparticles and nanothermite, *Combust. Flame*, 2022, **242**, 112170, DOI: 10.1016/j.combustflame.2022.112170.
16 J. McCollum, M. L. Pantoya and S. T. Iacono, Activating Aluminum Reactivity with Fluoropolymer Coatings for Improved Energetic Composite Combustion, *ACS Appl. Mater. Interfaces*, 2015, **7**, 18742–18749, DOI: 10.1021/acsami.5b05238.
17 S. L. Row and L. J. Groven, Smart Energetics: Sensitization of the Aluminum-Fluoropolymer Reactive System, *Adv. Eng. Mater.*, 2018, **20**, 1700409, DOI: 10.1002/adem.201700409.
18 G. Young, H. Wang and M. R. Zachariah, Application of nano-aluminum/nitrocellulose mesoparticles in composite solid rocket propellants, *Propellants, Explos., Pyrotech.*, 2015, **40**, 413–418.
19 Y. Zhou, K. Shi, M. Chowdhury, E. Hagen, Y. Wang and M. R. Zachariah, Direct microscopic imaging of exploding aluminum/nitrocellulose mesoparticles to reveal the enhanced combustion mechanism, *Fuel*, 2025, **387**, 134348, DOI: 10.1016/j.fuel.2025.134348.
20 M. A. Rubio, I. E. Gunduz, L. J. Groven, T. R. Sippel, C. W. Han, R. R. Unocic, V. Ortalan and S. F. Son, Microexplosions and ignition dynamics in engineered aluminum/polymer fuel particles, *Combust. Flame*, 2017, **176**, 162–171, DOI: 10.1016/j.combustflame.2016.10.008.
21 E. L. Dreizin and M. Schoenitz, Mechanochemically prepared reactive and energetic materials: a review, *J. Mater. Sci.*, 2017, **52**, 11789–11809.
22 T. M. Tillotson, A. E. Gash, R. L. Simpson, L. W. Hrubesh, J. H. Satcher Jr and J. F. Poco, Nanostructured energetic materials using sol–gel methodologies, *J. Non-Cryst. Solids*, 2001, **285**, 338–345.
23 K. K. Miller, J. L. Gottfried, S. D. Walck, M. L. Pantoya and C.-C. Wu, Plasma surface treatment of aluminum nanoparticles for energetic material applications, *Combust. Flame*, 2019, **206**, 211–213, DOI: 10.1016/j.combustflame.2019.04.042.
24 J. Kalman, D. K. Smith, K. K. Miller, S. K. Bhattacharia, K. R. Bratton and M. L. Pantoya, A strategy for increasing the energy release rate of aluminum by replacing the alumina passivation shell with aluminum iodate hexahydrate (AIH, *Combust. Flame*, 2019, **205**, 327–335, DOI: 10.1016/j.combustflame.2019.04.030.
25 S. Liu, M. Ye, A. Han and X. Chen, Preparation and characterization of energetic materials coated superfine aluminum particles, *Appl. Surf. Sci.*, 2014, **288**, 349–355, DOI: 10.1016/j.apsusc.2013.10.031.
26 L. Yang, E. Hagen, Y. Zhou, K. Shi, Y. Qin and M. R. Zachariah, Mechanism of how copper-coated nano-aluminum

 This journal is © the Owner Societies 2026

overcomes agglomeration and boosts air-breathing combustion of HTPB, *Combust. Flame*, 2026, **286**, 114799, DOI: 10.1016/j.combustflame.2026.114799.
27 Y. L. Shoshin, R. S. Mudryy and E. L. Dreizin, Preparation and characterization of energetic Al-Mg mechanical alloy powders, *Combust. Flame*, 2002, **128**, 259–269, DOI: 10.1016/S0010-2180(01)00351-0.
28 E. R. Wainwright, M. Inouye, M. Niu, K.-L. Chintersingh and T. P. Weihs, Comparing the ignition and combustion characteristics of ball-milled Al-based composites with Ti, Zr, and Mg additives, *J. Energ. Mater.*, 2023, **41**, 43–62.
29 P. P. K. Agarwal and T. Matsoukas, Synthesis and oxidation chemistry of highly energetic boron/aluminum/magnesium composites, *FirePhysChem*, 2023, **3**, 173–178, DOI: 10.1016/j.fpc.2023.03.001.
30 F. Maggi and F. Zadra, Combustion of Nanoaluminum and Magnesium in Fuel-Rich Propellants, *Propellants, Explos., Pyrotech.*, 2020, **45**, 724–729, DOI: 10.1002/prep.201900354.
31 Y. Yang and M. He, Thermodynamic cycle analysis of ramjet engines using magnesium-based fuel, *Aerosp. Sci. Technol.*, 2012, **22**, 75–84, DOI: 10.1016/j.ast.2011.06.005.
32 H. R. Pouretedal and M. H. Roudashti, Thermal behavior of metallic fuel pyrotechnics of Al, Mg and alloy of Al–Mg: a review, *J. Therm. Anal. Calorim.*, 2024, **149**, 12635–12650, DOI: 10.1007/s10973-024-13800-6.
33 C. E. Holley Jr. and E. J. Huber Jr., The Heats of Combustion of Magnesium and Aluminum1-3, *J. Am. Chem. Soc.*, 1951, **73**, 5577–5579, DOI: 10.1021/ja01156a020.
34 P. Ghildiyal, P. Biswas, S. Herrera, F. Xu, Z. Alibay, Y. Wang, H. Wang, R. Abbaschian and M. R. Zachariah, Vaporization-Controlled Energy Release Mechanisms Underlying the Exceptional Reactivity of Magnesium Nanoparticles, *ACS Appl. Mater. Interfaces*, 2022, **14**, 17164–17174, DOI: 10.1021/acsami.1c22685.
35 H. Wang, J. Shen, D. J. Kline, N. Eckman, N. R. Agrawal, T. Wu, P. Wang and M. R. Zachariah, Direct writing of a 90 wt% particle loading nanothermite, *Adv. Mater.*, 2019, **31**, 1806575.
36 Q. Meng, E. Hagen, C. Goodman, M. A. Foster and M. R. Zachariah, Simultaneous hyperspectral imaging and pyrometry for multi-phase temperature profiling of energetic composite reactions, *J. Quant. Spectrosc. Radiat. Transfer*, 2025, **346**, 109598, DOI: 10.1016/j.jqsrt.2025.109598.
37 A. Kramida, Y. Ralchenko and J. Reader, NIST Atomic Spectra Database (version 5.5.1), [Online]. Available: https://physics.nist.gov/asd, (2017). https://physics.nist.gov/asd.
38 W. G. Vincenti, C. H. Kruger Jr and T. Teichmann, *Introduction to physical gas dynamics*, 1966.
39 D. Nandy, Y. Singh, B. Shah and B. Sahoo, Transition properties of a potassium atom, *Phys. Rev. A: At., Mol., Opt. Phys.*, 2012, **86**, 052517.
40 K. Sullivan and M. Zachariah, Simultaneous Pressure and Optical Measurements of Nanoaluminum Thermites: Investigating the Reaction Mechanism, *J. Propul. Power*, 2010, **26**, 467–472, DOI: 10.2514/1.45834.
41 T. A. Brzustowski and I. Glassman, Vapor-Phase Diffusion Flames in the Combustion of Magnesium and Aluminum: I. Analytical Developments, in: *Heterog. Combust.*, ed. H. G. Wolfhard, I. Glassman and L. Green, Elsevier, 1964, pp. 75–115, DOI: 10.1016/B978-1-4832-2730-6.50009-9.
42 M. W. Chase, *et al.*, NIST-JANAF thermochemical tables, *J. Phys. Chem. Ref. Data*, 1998, **28**, 1951.
43 L. E. Fried, *CHEETAH: A fast thermochemical code for detonation*, Lawrence Livermore National Lab. (LLNL), Livermore, CA (United States), 1993, DOI: 10.2172/10154126.
44 S. Gordon and B. J. McBride, *Computer program for calculation of complex chemical equilibrium compositions and applications*, NASA Glenn Research Center, 1996.